Multiscale recurrence analysis of spatio-temporal data

M. Riedl,[1,a)] N. Marwan,[1] and J. Kurths[1,2]
[1]*Potsdam Institute for Climate Impact Research, 14473 Potsdam, Germany*
[2]*Department of Physics, Humboldt Universität zu Berlin, 12489 Berlin, Germany*

(Received 8 October 2015; accepted 20 November 2015; published online 10 December 2015)

The description and analysis of spatio-temporal dynamics is a crucial task in many scientific disciplines. In this work, we propose a method which uses the mapogram as a similarity measure between spatially distributed data instances at different time points. The resulting similarity values of the pairwise comparison are used to construct a recurrence plot in order to benefit from established tools of recurrence quantification analysis and recurrence network analysis. In contrast to other recurrence tools for this purpose, the mapogram approach allows the specific focus on different spatial scales that can be used in a multi-scale analysis of spatio-temporal dynamics. We illustrate this approach by application on mixed dynamics, such as traveling parallel wave fronts with additive noise, as well as more complicate examples, pseudo-random numbers and coupled map lattices with a semi-logistic mapping rule. Especially the complicate examples show the usefulness of the multi-scale consideration in order to take spatial pattern of different scales and with different rhythms into account. So, this mapogram approach promises new insights in problems of climatology, ecology, or medicine. © *2015 AIP Publishing LLC*.
[http://dx.doi.org/10.1063/1.4937164]

In many scientific disciplines, e.g., climatology, biology, ecology, and social sciences, the quantification of spatio-temporal dynamics is an important task in order to describe the observed dynamical system, for instance: the human brain activity which is strongly influenced by a hierarchical spatial organization of the brain tissue reaching from neurons to functional regions; or ecologic systems with large-scale interactions between the populations and the physical environment as well as short-scale ones among the organisms themselves. The investigation of such dynamics is still a challenge and the search for sufficient tools for this multi-scale analysis is still a topic of current research. A promising framework is the recurrence analysis where dissimilarities of paired timestamps of the recordings are successively used to display the complexity of the rhythms. In this work, we propose an extension of the recurrence approach based on mapograms enabling the separation of dynamical components of different spatial scales with their own complex rhythms. So, we are able not only to separate mixed regular patterns of specific scale and rhythm but also to reveal large-scale rhythms in pseudorandom fields and coupled map lattices (CMLs) beyond the dominant small-scale dynamics, which are new insides into underlying mechanisms of the observed spatial distributed systems.

I. INTRODUCTION

In many fields of science, e.g., climatology, biology, ecology, and social sciences, the analysis of spatio-temporal data is an important task quantifying and modeling the complex dynamics of the investigated systems. Especially the detection of different dynamical regimes plays an important role in this study, which is connected with a sufficient description of the observed behavior. Hence, it does not surprise that the development of analytical tools for this kind of analysis is still an important topic of the current research. In the majority of the known methods, this analysis is based on a pairwise comparison of pictures or matrices, resulting from a series of observations in order to uncover some temporal recurrence of spatial structures. Recent studies have shown that the framework of the recurrence analysis[1,2] is a promising approach for this task. So, Marwan *et al.*[3] proposed an extension of the recurrence plot (RP) for spatially distributed data, a generalized RP. Although this approach was originally designed for quantification of complex spatial structures, e.g., bone structure,[3] Turing structures, traveling waves in the Belousov Zhabotinsky reaction, satellite images of spatial chlorophyll distribution in oceans' colonies of plankton, fractals, snapshots of coupled map lattices, and structures in digital mammographic images;[4–8] the idea was also successfully applied to spatio-temporal data for detecting regime shifts in reaction diffusion models, e.g., the complex Ginzburg-Landau equation[9] and the Belousov-Zhabotinsky reaction.[10] In these applications, each time stamp of the two-dimensional systems is represented by measures based on the generalized RP, which resulted in time series of these measures, indicating changes in the spatial dynamics over time. But in most cases, this reduction of spatial information is too strong in order to analyze temporal recurrence of complex spatial patterns. Therefore, methods are needed which directly compare spatial structures. Fortunately, such approaches already exist. In ecology, the so-called kappa statistic[11] is often used for this purpose, and a modification of the Bhattacharyya similarity measure is popular in visual tracking.[12,13] A new idea has arisen that such global comparison of spatial structures might

a)maik.riedl@pik-potsdam.de

be embedded into the recurrence methodology for an improved description and quantification of spatio-temporal dynamics.[14,15] Agustí *et al.*[14] chose the spatiogram[12] in this way, whereas Marwan *et al.*[15] considered the distance of high dimensional state vectors representing the spatial structure in each time step. A disadvantage of the first method is the high level of abstraction where the spatial structure is approximated by a Gaussian peak. So, relevant patterns with a smaller scale than the size of the considered frame will be ignored. In contrast to that, the second approach resolves such finer patterns, but it is sensitive to noise or chaotic behavior because it strongly depends on the amplitude information. Another need for the analysis of such spatio-temporal data is the consideration of different spatial scales because of the possible superpositions of rhythms which are based on patterns of different spatial scales. Unfortunately, neither the spatiogram-based RP (SGRP, Appendix B) nor the high-dimensional RP (HDRP, Appendix C) provide such tuning feature for a multi-scale analysis.

Therefore, we propose here a novel use of the mapogram[13] in the recurrence methodology, the mapogram-based RP (MRP), in order to extend the use of the RP for a multi-scale analysis of spatio-temporal dynamics. In Sec. II, we introduce the algorithm of the mapogram and its use for a multi-scale analysis by means of the RP. In Sec. III A, this tool is applied to two rather simple examples, traveling waves and white noise, in order to illustrate the ability of this method to produce the expected recurrence patterns, which are known from the classical RP approach. Further, examples of superposed spatio-temporal dynamics are investigated, in Sec. III B, to motivate a multi-scale analysis by means of the mapogram. In Sec. III C, this motivation is accentuated by the analysis of a more practical and complex example, a coupled map lattice with semi-logistic mapping rule[16] modeling the dynamics of spatially distributed populations. Finally, summary and conclusion are given in Sec. IV.

II. METHOD

In this section, we introduce the mapogram which we propose for extending the spatio-temporal analysis by means of the RP approach. The aim of this method is a pairwise comparison of two-dimensional data fields and the quantification of their similarity (an extension to three or even higher dimensions is straightforward). The data fields consist of the same set of elements of a two dimensional vector space. To each element, the value of a feature (quantity, measure, or property) is assigned, which might be different in both data fields. Formally, such data field is given by $F = \{f_{ij}\}_{i=1,\ldots,N_i;j=1,\ldots,N_j}$, where i and j are the indexes of the elements and f_{ij} the assigned values of the feature. $N = N_i * N_j$ is the number of the field elements. The first step of the mapogram is a simplification of the variation of f_{ij} by means of a histogram

$$n_b = \sum_{i=1}^{N_i}\sum_{j=1}^{N_j} g_b(f_{ij}), \tag{1}$$

where the binary matrices g_b resulted from

$$g_b(f_{ij}) = \begin{cases} 1 & f_{ij} \in \text{b-th bin} \\ 0 & \text{otherwise.} \end{cases} \tag{2}$$

$b = 1, \ldots, B$ is the index of the histogram's bins, B disjoint right side closed intervals which fully cover the range of f_{ij} or a contiguous part of it. So, n_b is the number of elements with values in the b-th bin. The $N_i \times N_j$ binary matrices are normalized

$$m_{b,i,j} = \frac{g_b(f_{ij})}{n_b} \tag{3}$$

and convoluted with a kernel function K_γ, the blurring, which leads to the mapogram. This spatial smoothing is done for each $m_{b,i,j}$ and is controlled by the positive definite non-zero parameter γ, the bandwidth of the kernel given in units of sample points

$$m_{b,\gamma,i,j} = \sum_{i'=1}^{N_i}\sum_{j'=1}^{N_j} m_{b,i',j'} K_\gamma\left(\frac{||(i',j') - (i,j)||}{\gamma}\right). \tag{4}$$

In the original approach, Nilsson[13] used a Gaussian kernel. For an easier interpretation of the relationship between the kernel's bandwidth and the considered spatial scale, we use instead the Epanechnikov kernel,[17] which has a bounded domain of non-zero elements

$$K_\gamma(x) = \frac{3}{4\gamma^2}(1 - x^2)\mathbf{I}(x). \tag{5}$$

x is the normalized spatial distance between the points (i, j) and (i', j') and $\mathbf{I}(x)$ is the indicator function, which is equal to the unity for $|x| \leq 1$ and otherwise zero. As in the spatiogram (see Appendix B, Eq. (B4)), the similarity between the two fields is calculated by a weighting of the Bhattacharyya coefficient, here

$$S^m_{f,f'}(\gamma, B) = \sum_{b=1}^{B} \sqrt{\frac{n_b n'_b}{\left(\sum_b n_b\right)\left(\sum_b n'_b\right)}} \times \sum_{i=1}^{N_i}\sum_{j=1}^{N_j} \sqrt{\frac{m_{b,i,j,\gamma} m'_{b,i,j,\gamma}}{\left(\sum_{ij} m_{b,i,j,\gamma}\right)\left(\sum_{ij} m'_{b,i,j,\gamma}\right)}}, \tag{6}$$

where the second factor is the weight. The range of the similarity measure is from 0 to 1, respectively, fully dissimilar and equal data fields. For $\gamma \to 0$, the $m_{b,\gamma,i,j}$ (Eq. (4)) tends to $m_{b,i,j}$ (Eq. (3)). In the limes $\gamma = 0$, the similarity measure is set to

$$S^m_{f,f'}(0, B) = \sum_{b=1}^{B} \sqrt{\frac{n_b n'_b}{\left(\sum_b n_b\right)\left(\sum_b n'_b\right)}} \sum_{i=1}^{N_i}\sum_{j=1}^{N_j} \sqrt{m_{b,i,j} m'_{b,i,j}}, \tag{7}$$

which corresponds to the κ-statistics.[11] In the following text, this unblurred version of the mapogram approach, the lowest level of blurring, is indicated by $\gamma = 0$. In relation to that, the

highest level of blurring is marked by $\gamma = \infty$, which corresponds to $S^m_{f,f'} = 1$ for the blurred mapogram (Eq. (6)). Further details can be found in Nilsson *et al.*[13]

The parameters of the mapogram are the kind of binning for the histogram and the strength of blurring: (i) The aim of this binning is a simplification of the variations of the values in the data field. There are global and local binning schemes. In the global scheme, there are bins which are equal for the compared data fields. In contrast to that, the local scheme depends on the distribution of each single data field and resulted in different bins for both ones. The number of the bins is strongly connected to the size of the bins and the resulting resolution of the variation. In this work, we only use the global scheme, in order to keep the example as simple as possible. (ii) The choice of the blurring coefficient γ is less complicated, since two-times of its value correspond to the minimal spatial scale of patterns which will be considered (cf. Appendix A). So, the blurring has properties of a low pass filter. This is used to tune the spatial scale in a multi-scale analysis and can be stressed by constructing a bandpass like version by using

$$\Delta S^m_{f,f'} = S^m_{f,f'}(\gamma_2, B) - S^m_{f,f'}(\gamma_1, B), \tag{8}$$

where γ_1 and γ_2 ($\gamma_1 < \gamma_2$) correspond to the smallest and the highest spatial scale, respectively, of the considered band.

The aforementioned extension to 3D is done by considering a three-dimensional data field (Eq. (1)) and the use a three-dimensional kernel function (Eq. (5)). Then, the resulting binary matrices (Eq. (3)) and their blurred versions (Eq. (4)) are also three-dimensional. Taking the higher-dimension into account, the summation over two indexes (Eqs. (1), (4), (6), and (7)) is replaced by a summation over three ones.

The similarity measures of the mapogram, the spatiogram, and the kappa statistic take the spatial variability into account. For application to spatial-temporal dynamics, we will use these tools in the framework of the RP analysis in order to investigate the temporal evolution of the spatial variability. For this purpose, an RP is constructed based on the mentioned similarity measures. Let us assume that the data come from repeated measurements of a spatially distributed system. Further, the measure for each timestamp results in a two-dimension field of values F_t. These snapshots of the spatial dynamics are pair-wise compared by means of a similarity measure leading to the similarity matrix $S_{t,t'}$, which gives the similarity of the snapshots at the time points t and t'. If $S_{t,t'} > \epsilon$, then both snapshots are assumed as similar and the corresponding entry of the binary recurrence matrix is set to one

$$R_{t,t'}(\epsilon) = \Theta(S_{t,t'} - \epsilon). \tag{9}$$

Θ denotes the Heaviside function which is 1 for values greater than zero and 0 otherwise. There are several strategies to select a sufficient value of the threshold.[2] It could be globally set by a portion of the maximum phase space diameter or locally, fixing the number of neighbors of the single points. In this work, we fix the recurrence rate to 10%.

After this conversion, we can use the full power of the established recurrence quantification analysis and recurrence network analysis[2,18] for the investigation of the temporal evolution of the spatial patterns. For example, there might be a quantification of the diagonal lines, which fulfill the condition

$$(1 - R_{i-1,j-1})(1 - R_{i+l,j+l}) \prod_{k=0}^{l-1} R_{i+k,j+k} \equiv 1. \tag{10}$$

The histogram of their lengths is used to calculate the measure determinism *DET*, which is defined by

$$DET(\epsilon, l_{min}) = \frac{\sum_{l=l_{min}}^{N} lH(l)}{\sum_{l=1}^{N} lH(l)}. \tag{11}$$

It is the fraction of points in the RP which are organized as diagonal lines expressing the regularity or predictability of the observed dynamics. $H(l)$ is the histogram of their lengths and l_{min} is a minimal length that can be set up to reduce the influence of tangential motion.[2] We set l_{min} to 3, the smallest length of a line which covers not only the case of regular oscillation but also chaotic behavior where only short lines are expected.

III. APPLICATION

A. Simple basic models

1. Waves

First, we apply the MRP to a simple but basic example of spatio-temporal dynamics. We start with parallel traveling waves in the plane, which are constructed by

$$f(x, y, t) = A \sin\left(\frac{2\pi}{T} y + vt\right) \tag{12}$$

for all x. The parameter T defines the spatial scale of the pattern (i.e., the distance between successive maxima in y-direction), whereas v determines the velocity of the temporal change of the pattern, the moving from up to down. So, the temporal recurrence is given by $2\pi/v$. In the examples, the sampling points are 1, 2,…, 100 for x, y, and t. Snapshots of simulations, the resulting spatial patterns, are shown in Fig. 1 for different values of T. The velocity v is 0.5 rad per time step. Applying the MRP, we expect a RP with lines parallel to the main diagonal as in the classical RP of a harmonic oscillation. For comparison for the HDRP, the unblurred mapogram-based RP (UMRP), and the SGRP are shown in Fig. 2. The plots (Fig. 2) indicate that the HDRP ($DET \approx 0.97$), the SGRP ($DET \approx 0.92$), as well as the UMRP ($DET \approx 1$) are able to produce the expected structure of diagonal lines as the classical approach in the case of one-dimensional harmonic oscillations.

2. White noise

The second example is white noise which is used as counter example where the plot shows no regularities. Let us

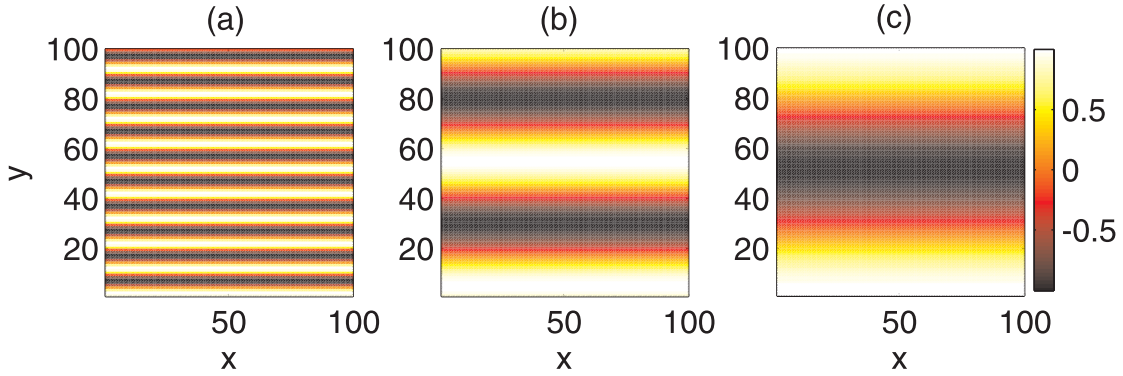

FIG. 1. Snapshots of the parallel waves of Eq. (12) which travel from top to the bottom of a 100×100 data field. The different scales of the spatial patterns are determined by (a) $T = 10$, (b) $T = 50$, and (c) $T = 100$.

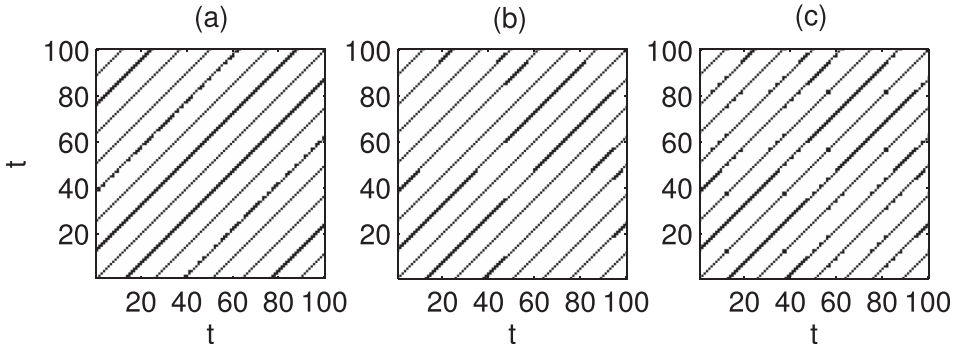

FIG. 2. RPs of travelling waves shown in Fig. 1. The scale of the spatial pattern is $T = 50$ and the velocity is $v = 0.5$ rad per time step. The plots are (a) the HDRP, (b) the UMRP, and (c) the SGRP. The recurrence rate is set to 0.1. For the UMRP and the SGRP there are two bins $\{(-\infty, 0], (0, \infty]\}$.

consider a series of 100×100 matrices where the values of the elements are realizations of independent normally distributed random numbers $N(0, 1)$. As in the previous example, the different methods for recurrence analysis of spatio-temporal data are applied (Fig. 3). They show that only the use of the UMRP leads to the expected scattered points (Fig. 3(b), $DET \approx 0.01$). In the other cases, there are vertical and horizontal structures (Figs. 3(a) and 3(c), $DET \approx 0.02$ and $DET \approx 0.04$, respectively), which indicate more frequent realizations of the random field. A reason of such structures could be an interaction of the algorithm of the pseudorandom generator (MATLAB 2012b, The MathWorks, Inc.) with the filling procedure of the 3D-datafield (2 spatial plus 1 time dimension). The comparison of HDRP and UMRP in Figs. 3(a) and 3(b), respectively, visualize that a digitalization neglects these problems on small scales of the 2D random matrices. On larger scales, this clustering appears again as shown in the SGRP (Fig. 3(c)) which points out the advantage of a multi-scale analysis in order to separate components of spatio-temporal dynamics. In the following, the advantage of this multi-scale analysis by means of the blurred mapogram-based RP (BMRP) is putted over in Sec. III B and III C applying it to other examples of spatio-temporal dynamics.

B. Superposed dynamics—Example of multi-scale approaches

1. Superposed waves

The aim of multi-scale approaches is the separation of components of superposed dynamics in order to distinguish the underlying mechanisms. Let us stress the example of traveling waves (Eq. (12)). We add two instances with different spatial scales T_1 and T_2 and velocities v_1 and v_2. The first component is defined by $A_1 = 1$, $v_1 = 0.3$, and $T_1 = 14$. The moving direction is changed to a horizontal one exchanging y by x in Eq. (12). So, the recurrence time of a spatial pattern is $2 * \pi / v_1 \approx 20$. The second component is given by $A_2 = 0.5$, $v_2 = 0.2$, resulting in a recurrence time

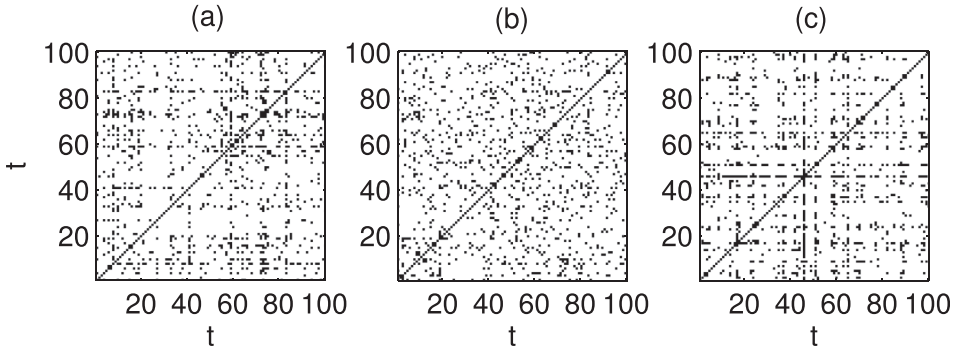

FIG. 3. RPs of a run of 100 data fields of the size 100×100 with realizations of independent normally distributed random numbers $N(0, 1)$. The plots are (a) the HDRP, (b) the UMRP, and (c) the SGRP for the same run. The recurrence rate is set to 0.1. For the UMRP and the SGRP, the range of the values are divided into 10 equally sized bins.

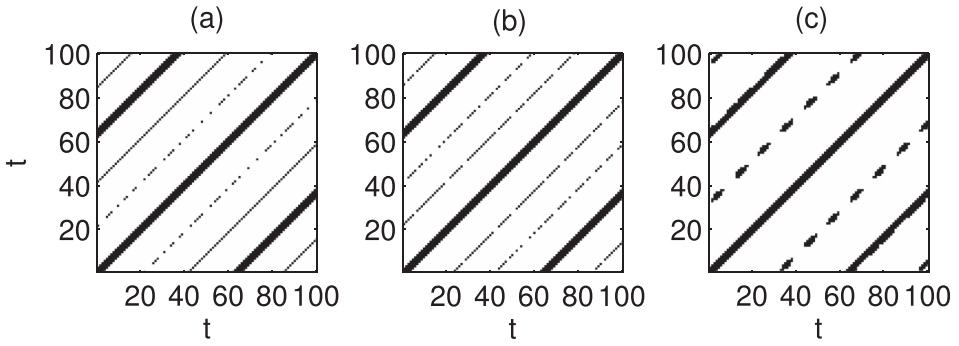

FIG. 4. Different RPs of a superposition of two examples of Eq. (12). The first component moves from right to left ($A=1$, $T=14$, and $v=0.3$). The second component moves from up to down ($A=0.5$, $T=50$, and $v=0.2$). There is (a) the HDRP, (b) the UMRP ($\gamma=0$; bins: $\{[-\infty,-0.5],(-0.5,0.5],(0.5,\infty]\}$), and (c) the BMRP ($\gamma=15$; bins: $\{(-\infty,-0.5],(-0.5,0.5],(0.5,\infty]\}$). The recurrence rate is set to 0.1.

of $2*\pi/v_2 \approx 30$ and $T_2=50$. Its moving direction is the same as defined in Eq. (12). Because of the higher amplitude, the first component is the dominant one in the whole dynamics. The resulting HDRP (Fig. 4(a), $DET \approx 0.96$) displays the expected diagonal line structure of the dominant dynamics indicated by the vertical distance of the diagonal lines, which is equal the recurrence time of about 21. The second rhythm is encoded by thicker lines at a distance of the least common multiple of the recurrence times of both single components, about 60. In order to distinguish both components, we applied the MRP with the blurring coefficient equal to 0 and 15 to the data (Figs. 4(b) and 4(c), $DET \approx 0.97$ and $DET \approx 0.97$, respectively). The UMRP (Fig. 4(b)) leads to a RP like the HDRP. The use of a blurring coefficient of 15 reveals the expected diagonal line structure of the 2*nd* harmonic component with a distance of the diagonal lines of about 30. Let us switch the dominance of both components by switching the amplitude values ($A_1=0.5$ and $A_2=1$). The resulting RP are shown in Fig. 5. The HDRP and the use of the UMRP (Figs. 5(a) and 5(b), $DET \approx 0.97$ and $DET \approx 0.98$, respectively) now only display the diagonal structure of the superposed dynamics. The use of BMRP uncovers the second component too (Fig. 5(c), $DET \approx 1$), but the rhythm of the first part is masked by diagonal lines with a distance of 60, which is again the least common multiple of the separated component (30) and the covered one (20). The band-pass version of the mapogram approach (Eq. (8)) solves the problem. We consider the mapograms with $\gamma_1=0$, $\gamma_2=15$, and $\gamma_3=\infty$, where S is equal 1 by definition for γ_3. The resulting bands of the spatial scale are $[0-30]$ (Eq. (8), γ_1 and γ_2) and $[30-\infty]$ (Eq. (8), γ_2 and γ_3). Setting the ΔS of Eq. (8) into Eq. (9), we get Figs. 6(a) and 6(b) ($DET \approx 1$ and $DET \approx 0.98$, respectively). Ignoring the main diagonal in panel (a), the distance between the other lines is about 20 and 40, the recurrence time and a multiple of it, respectively, of the first component. As expected the spatial scale ($T=14$) of the indicated component lies in the considered band $[0-30]$. In panel (b), the distance is about 30 reflecting the recurrence time of the second component. Here, the spatial scale of the uncovered dynamic ($T=50$) is in the considered band $[30-\infty]$, too.

2. Additive noise

Next we add noise to traveling waves of Eq. (12) ($T=20$, $v=0.5$, and $A=1$) in order to study the robustness of the MRP. We take white noise which consists of a set of pairwise independent Gaussian distributed random numbers. The signal-to-noise ratio is set to 0.1. Fig. 7 displays the resulted HDRP, UMRP, and BMRP for $\gamma=2$ ($DET \approx 0.24$, $DET \approx 0.07$, and $DET \approx 0.29$, respectively). All panels clearly show the expected diagonal line structures in spite of a high noise. But we also see vertical and horizontal structures in HDRP (Fig. 7(a)). We remember the artifacts for the example of pure white noise (Fig. 3). In order to separate the periodic patterns and the noisy components, we applied the band-pass version of the mapogram as in the preceding example (Figs. 8(a)–8(c), $DET \approx 0.05$, $DET \approx 0.26$, and $DET \approx 0.02$, respectively). Here, the bands of spatial scale are: $[0-4]$ ($\gamma_1=0$, $\gamma_2=2$, Eq. (8); panel (a)), $[4-30]$ ($\gamma_1=2$, $\gamma_2=15$, Eq. (8); panel (b)), and $[30-\infty]$ ($\gamma_1=15$, $\gamma_2=\infty$, Eq. (8); panel (c)). We find now a clear separation of the expected recurrence pattern of white noise, the traveling waves, and the artifacts of the pseudo random generator. So, the multi-scale approach by MRP gives not only a separation of different dynamical components but also the scale of their corresponding spatial patterns which is reflected by the selected bands.

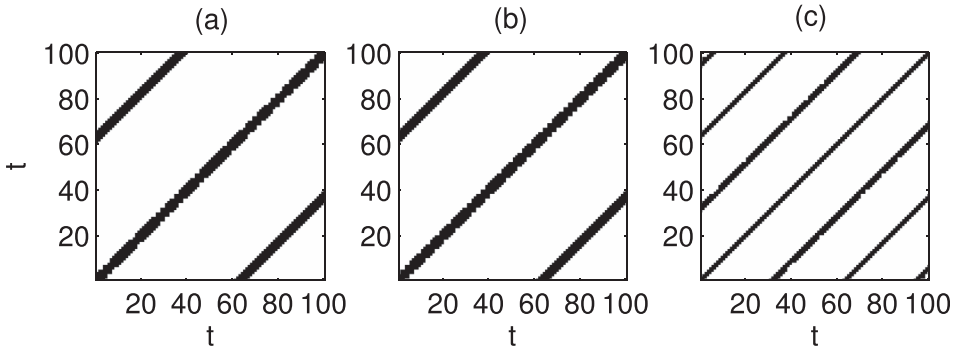

FIG. 5. Different RPs of a superposition of two examples of Eq. (12). The first component moves from right to left $A=0.5$, $T=14$, $v=0.3$). The second component moves from up to down ($A=1, T=50$, and $v=0.2$). There is (a) the HDRP, (b) the UMRP ($\gamma=0$; bins: $\{[-\infty,-0.5],(-0.5,0.5],\ (0.5,\infty]\}$), and (c) the BMRP ($\gamma=15$; bins: $\{(-\infty,-0.5],(-0.5,0.5],\ (0.5,\infty]\}$). The recurrence rate is set to 0.1.

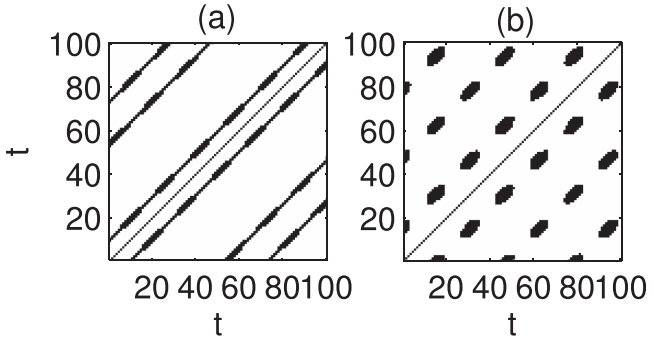

FIG. 6. RPs for the example of Fig. 5. It bases on the band-pass version of the mapogram (Eq. (8)) with $\gamma_1 = 0$ and $\gamma_2 = 15$ (a); and $\gamma_1 = 15$ and $\gamma_2 = \infty$ (b). The other parameters are the same as in Fig. 5.

C. Spatial chaos

In this section, we will consider another complex spatio-temporal dynamics in order to illustrate the use of the MRP in a more practical multi-scale analysis. We analyze a CML with a semi-logistic mapping rule. This model is defined by a regular square lattice ($\{i, j\}$, $i = 1, \ldots, N$, $j = 1, \ldots, N$), the states of the nodes $X_{ij} \in [0, 1]$, and a rule for updating the states. The size of the lattice is set to 120×120 where only the central lattice of 100×100 is analyzed in order to avoid possible edge effects. At each time step the X_{ij} are synchronously updated according to the set of rules which involves interactions between neighboring nodes

$$X_{ij}^{n+1} = rY_{ij}^{n}(1 - Y_{ij}^{n}), \tag{13}$$

$$Y_{ij}^{n} = \frac{1}{\{\Omega\}} \sum_{(i,j)\in\Omega} X_{ij}^{n}. \tag{14}$$

Here, the neighborhood Ω contains the target node (i, j) and the 8 surrounding ones if the target node is a central one. In the case of nodes of the boundaries, the number of neighbors is adapted. Dzwinel[16] proposed this model for a description of the growth of spatial distributed populations. The analysis of this model showed that there is an accumulation point at $r \approx 3.5699$, i.e., the onset of chaos. For lower values of the control parameter r, the author found a cascade of period doubling as in the original logistic map where the states converge quickly to uniform and synchronized nodes. Surprisingly, higher values resulted in a cascade of band merging instead of the chaotic behavior of the one-dimensional map. Further the states variance increase, i.e., the X_{ij} diversifies progressively and irregular spatial clusters, representing the evolution of complex spatial structures, can be observed. Dzwinel concluded that the global chaotic temporal behavior is transferred into spatial chaos. This dynamics finally stabilizes for $r > 3.9$ in a regime where the mean $\langle X_{ij} \rangle$ fluctuates around the fixed point ($X^* \approx 2/3$). For illustration, we show the bifurcation diagram (Fig. 9) and examples of time steps for different values of the control parameter r (Fig. 10). The question is how this spatial chaos looks like? We focus on the range $3.7 \leq r \leq 3.9$, for example, to answer this question. For the values of $r = 3.70$, $3.71, 3.72, \ldots, 3.9$, we simulate runs of length 100 000 time steps eight times where the initial conditions were realizations of a random field. The last 100 time steps of each run are used to construct the RP by means of the mapogram with $\gamma = 0, 5, 10, 15, \ldots, 50$, a multi-scale approach. The domain was split into 64 bins, as recommended by Dzwinel, and the recurrence rate was set to 0.1. Typical recurrence patterns are shown in Fig. 11 which are simultaneously found in each simulation, i.e., for each selected value of r, corresponding

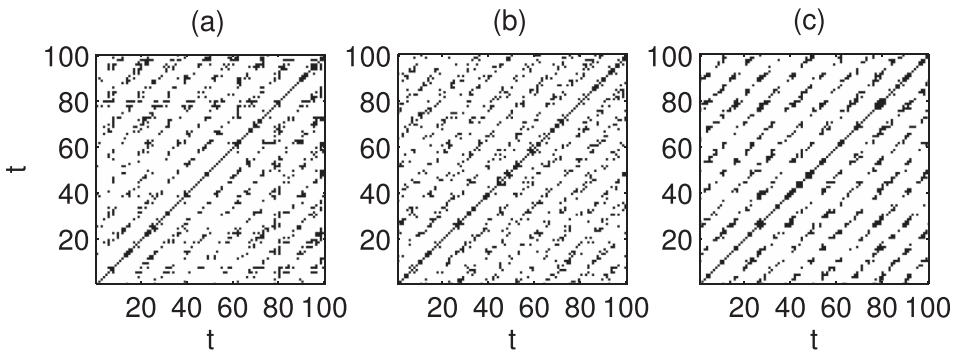

FIG. 7. Recurrence analysis of the dynamics of parallel waves with additive noise which travels from top to the bottom of a 100×100 data field (Eq. (12), $T = 20$, $v = 0.5$ rad per time step). Panel (a) displays an example of the resulted HDRP whereas (b) and (c) show the MRPs (respectively, $\gamma = 0$ and $\gamma = 2$; bins: $\{(-\infty, 0], (0, \infty]\}$). The signal-to-noise ratio is 0.1, and the recurrence rate is 0.1.

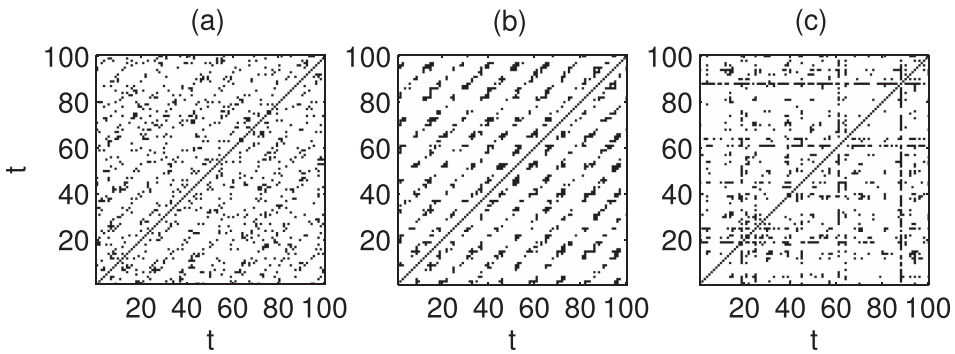

FIG. 8. RPs for the example of Fig. 7. It bases on the band-pass version of the mapogram (Eq. (8)) with (a) $\gamma_1 = 0$ and $\gamma_2 = 2$, (b) $\gamma_1 = 2$, $\gamma_2 = 15$, and (c) $\gamma_1 = 15$ and $\gamma_2 = \infty$. The other parameters are the same as in Fig. 5. The three plots reflect the different components of the spatio-temporal dynamics: (a) the noise, (b) the periodic pattern, and (c) long-term artifacts of the pseudo-random generator.

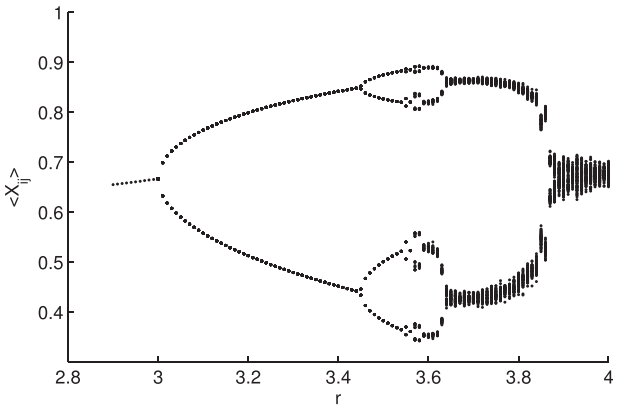

FIG. 9. Bifurcation diagram of the CML (Eqs. (13) and (14)). The size of the lattice is 120×120 data points. For each considered value of r, there was a run of 100 000 iterations. A point represents the spatial means of the inner elements of the lattice (100×100) neglecting boundary effects. For each run (value of r) only the last 100 iterations are considered to avoid transient behavior.

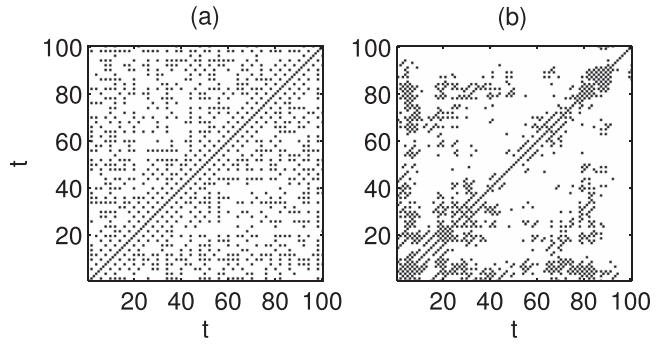

FIG. 11. MRPs of realizations of the CML ($r = 3.78$). The domain $[0, 1]$ is divided into 64 equal sized bins. The blurring coefficients are (a) $\gamma = 0$ and (b) $\gamma = 50$.

to different scales of the considered spatial patterns. In Fig. 11(a), we consider small spatial scales by choosing $\gamma = 0$. The RP reveals a drift of the recurring patterns, i.e., we find regular structures near the main diagonal which change to noise like structures for regions more far from the center. The periodicity of this regular recurrence structure near the main diagonal changes from a period of four for $r = [3.7, 3.86]$ to a period of two for $r = [3.87, 3.9]$. The period of four shows that the four arms of the bifurcation diagram (for $r = 3.6$, for example, in Fig. 9) still exist but merge into two arms for $r = [3.7, 3.86]$, if we focus on spatial patterns of smaller scales. Despite the regular structure in the RPs of small scale spatial patterns, the determinism is $DET = 0$, instead of an expected high value, because of the empty odd columns of the RP avoiding diagonal lines. These empty columns indicate that in one of the two arms of the bifurcations diagram (for $r = [3.7, 3.86]$ in Fig. 9) the small spatial patterns never recur. In Fig. 11(b) ($DET \approx 0.59$), we consider large spatial scales by setting $\gamma = 50$. Here, the RP shows an irregular occurrence of shorter diagonal lines as well as white bands and rectangle like structures. It is related to large spatial scales and, respectively, visualizes chaotic behavior and different attractors. In the range of smaller spatial scales, there is a periodic change of columns in the RP where snapshots recur and where snapshots do not recur (Fig. 11(a)). This pattern can be observed for $3.7 \leq r \leq 3.88$ and relates to the upper and the lower branch of the bifurcation diagram (Fig. 9), respectively. This recurrence pattern and that one of the larger spatial scales can be easily distinguished by the quantity *DET* (Eq. (11)). That means the two-periodic changes of the recurrence leads to a value of 0, whereas the other one is characterized by a non-zero value. The black region in Fig. 12(a) ($DET = 0$) shows the spatial scale where the two-periodic change of the recurrence can be observed. Obviously, the structure vanishes for a higher level of blurring, while the threshold of the disappearance successively decreases until $r = 3.86$. That indicates a decreasing scale of this spatial pattern, which shows this recurrence structure. The outlier at $r = 3.83$ (window of period 3 in the logistic map) resulted from one of the eight runs where the period of 4 time steps appears. With the disappearance of the two-periodic change of recurrence, recurrence patterns of chaotic behavior appear (e.g., Fig. 11(b)). The light band along the border of the black region in Fig. 12(a) indicates the scale of the underlying spatial pattern, which decreases with rising values of the control parameter. In this example, we focus on the region $r \geq 3.7$. A consideration of lower values, $3.57 \leq r \leq 3.7$, needs a higher resolution of the closed interval between 0 and 1 because the size of the single branches decreases with decreasing values of the control parameter and the branches have to be covered by more than one bin in order to describe the rhythm. A reduction of the bin size could be one solution for this problem but leads to an increased number of bins which have to be compared and to a smaller filling of the bins reducing the significance of the bins. This rise of computational steps resulted in a longer operation time. Another strategy is the use of non-equally

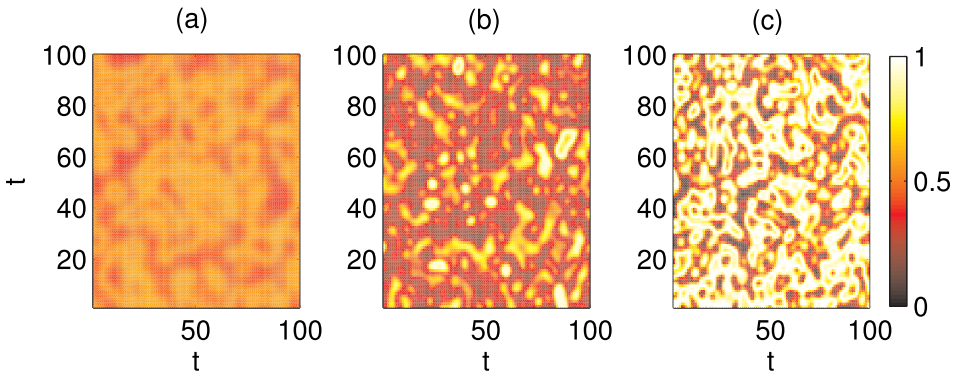

FIG. 10. Snapshots of realizations of the CML (Eqs. (13) and (14)). The simulation parameter are the same as in Fig. 9 except the controlling parameter: (a) $r = 3.6$, (b) $r = 3.8$, and (c) $r = 4$.

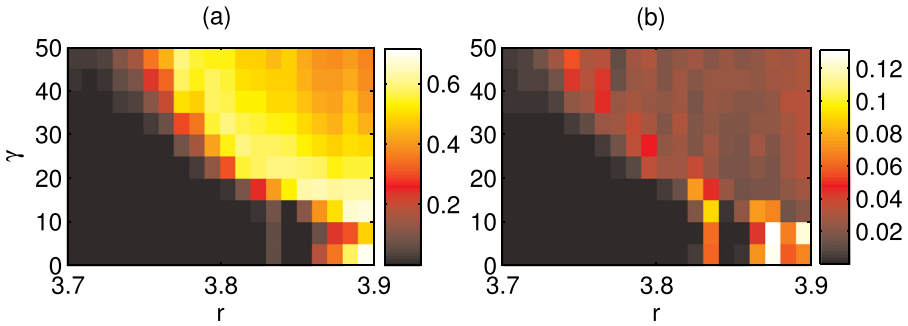

FIG. 12. Statistics of *DET* (Eq. (11)) depending from the control parameter r of the model and the blurring coefficient γ of the MRP (binning: 64 equal sized bins). (a) The mean and (b) its error (standard deviation divided by the square root of 8) are calculated from 8 runs for each value of the control parameter. The light band shows that with increasing r the scale of the pattern showing chaotic behavior decreases.

sized bins, which are locally defined for each time step. But this more detailed investigation is outside the focus of this paper and will be done in future works.

IV. CONCLUSION

In summary, we have proposed an extension of the recurrence plot approach, the MRP, which allows a multi-scale analysis of spatio-temporal data. The application to traveling waves in the plane shows that the MRP is able to reproduce the results of the other recurrence tools in the case of only one dynamical component. For two superposed components, the new method separates both, which is not possible with the other approaches. Further the application to more complex examples, such as additive noise and spatial chaos, leads to new insides into the underlying mechanism, i.e., long term correlations and gradual decrease of the spatial scale of the rhythmic pattern, respectively.

In particular, the simple example of traveling waves shows that the MRP produces the diagonal structures of a regular oscillation as the HDRP (Fig. 2). But there is no equivalence between UMRP and HDRP, which is indicated by the example of pure noise (Fig. 3). The differences are rather an indicator for more than one dynamical component, which is proved by the separation in the example of additive noise. A major cause of the different results is the simplification of the spatial pattern by means of the histogram in the MRP. Here, the discretization proves its usefulness for the investigation of complex dynamics as in the field of symbolic dynamics. Furthermore, the example of composed traveling waves shows that we have to distinguish two cases. If the components partitions on the resulted variance successively decrease and the corresponding spatial scales of the components increase, then the low pass property of the BMRP is sufficient to separate the parts (Fig. 4). Otherwise, the band-pass like version of the BMRP has to be used, since the dominant component covers the underlying part with the smaller spatial scale in the original BMRP (Figs. 6 and 5, respectively). Surprisingly, the separation in the case of additive noise by means of this band-pass like version of BMRP offers a way to visualize the quality of pseudorandom generators (Fig. 8). There are many quantities evaluating the quality of pseudorandom generators, which include statistics[19] as well as quantities from RP analysis and information theory.[20] But we do not know any algorithm that uses a regular arrangement of a series of pseudorandom numbers in a 3D matrix in order to reveal regularities coming from the construction algorithm. So, this way of sorting and the use of the multi-scale analysis by means of BMRP could be a new ansatz in future studies concerning the evaluation of pseudorandom numbers. The potential of the multi-scale analysis of spatio-temporal dynamics by means of BMRP is underlined by the application to the CML. Here, we could show that the spatial chaos, stated by Dzwinel,[16] has different spatio-temporal components where their spatial scales are controlled by the model parameter. But this example also elucidates a critical point of the MRP that is the selection of the center and the size of the bins. In contrast to the straightforward use of the blurring coefficient for the determination of the minimal resolved spatial pattern, the binning does not only depend on the observed systems state space but also on the focus of the observer her/himself. As in the theory of symbolic dynamics, decreasing bin sizes leads to increasing resolutions, i.e., accuracy. In the case of a state space with regions of different fine structure as in the last example, the use of adaptive bin sizes is recommended. We do not illustrate the influence of instationarities, e.g., trend, but here the solution could be the use of a binning depending on each time step, for example, the definition of the bin edges by percentiles of each snapshot.

All in all, the proposed MRP and its use in multi-scale approach promises a more detailed description of spatio-temporal dynamics in comparison to the aforementioned tools which might help to answer questions from the scientific fields of climatology, ecology, plasma physics, and medicine, for example.

ACKNOWLEDGMENTS

This work was supported by the Volkswagen Foundation (Grant No. 88462) and the DFG RTG 2043/1 "Natural Hazards and Risks in a Changing World."

APPENDIX A: SPATIAL SCALE AND BLURRING

Let us analyze the connection between the blurring and the scale of the observed spatial pattern. We consider the low pass filter effect of the blurring from another point of view. Instead of noise reduction, here we investigate the ability to cut-off spatial pattern with a smaller scale than a threshold. As mentioned in the Introduction, this opportunity of tuning is the great advantage of the novel tool in comparison to the other approaches. Let us consider striped pattern which resulted from snapshots of traveling waves (Eq. (12)). The parameters are $T = 5, 10, \ldots, 100$ and $v = 0.5$. For each value of T, we compared the snapshot with its 90° rotated version. The different orientation should clearly reduce the

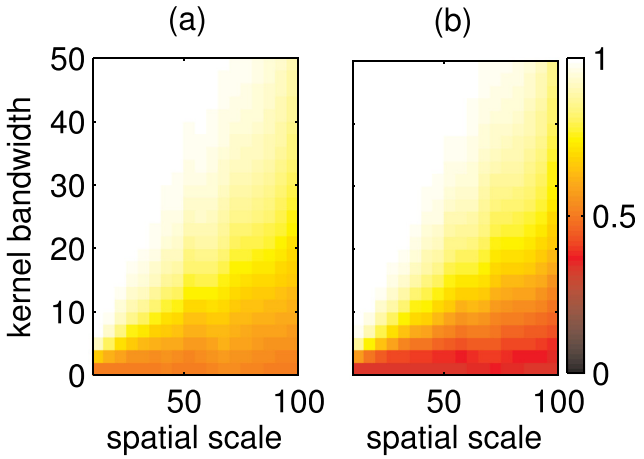

FIG. 13. The similarity measure (Eqs. (6) and (7)) of the comparisons between instances of Eq. (12) ($T = 5, 10, \ldots, 100$, $v = 0.5$) and their 90° rotated versions in relation to the level of blurring which is given by the kernel bandwidth $\gamma = 0, 2, \ldots, 50$ (Eq. (5)). The values of the similarity measures are color coded. The number of bin is 2 ($\{(-\infty, 0], (0, \infty]\}$ panel (a)), and 3 ($\{(-\infty, -0.5], (-0.5, 0.5], (0.5, \infty]\}$ panel (b)).

similarity $S^m_{f,f'}$ (Eqs. (6) and (7)) of both. That is the striped pattern induces this difference, so its blurring should lead to an increase in $S^m_{f,f'}$. We calculate $S^m_{f,f'}$ for different values of the blurring parameter, $\gamma = 0, 2, \ldots, 50$, in order to find the point where the differences between the compared snapshots vanish in relation to T (Fig. 13). The edge between the white region and the gray one indicates the cutoff characteristic of the blurring. It shows that the blurring fully remove spatial patterns with scales which are smaller than twice of the value of the blurring parameter γ. Further, the comparison of Figs. 13(a) and 13(b) indicates that this cutoff relation is less affected by the number of bins.

APPENDIX B: SPATIOGRAM BASED RECURRENCE PLOT

We start with a field $F = \{f_{ij}\}_{i=1,\ldots,N_i;j=1,\ldots,N_j}$ and build its histogram by means of the binary matrices in Eq. (2). Based on these binary matrices, the mean index of the elements in the b-th bin is calculated by

$$\mu^i_b = \frac{1}{n_b}\sum_{i=1}^{N_i}\sum_{j=1}^{N_j} i g_b(f_{ij}), \tag{B1}$$

$$\mu^j_b = \frac{1}{n_b}\sum_{i=1}^{N_i}\sum_{j=1}^{N_j} j g_b(f_{ij}). \tag{B2}$$

Further, the covariance of the indexes is given by

$$\sigma_b = \frac{1}{n_b - 1}\sum_{i=1}^{N_i}\sum_{j=1}^{N_j}\begin{pmatrix} (i-\mu^i_b)^2 & (i-\mu^i_b)(j-\mu^j_b) \\ (i-\mu^i_b)(j-\mu^j_b) & (j-\mu^j_b)^2 \end{pmatrix} g_b(f_{ij}). \tag{B3}$$

The triple $(n_b, (\mu^i_b, \mu^j_b), \sigma_b)$ represents the spatial distribution of the field elements in the b-th bin. That is, the spatial distribution is assumed as the two dimensional Gaussian distribution $N((\mu^i_b, \mu^j_b), \sigma_b)$. In the case of an empty bin or a bin with only one element, the triple is set to $(0, (0, 0), 0)$ and $(1, (ij), 0.5)$, respectively, where 0.5 is the minimal variance in the case of two neighboring field elements. The ensemble of triples is called spatiogram. Based on this, the similarity between two fields, $F(t)$ and $F(t')$, is quantified by the weighted Bhattacharyya coefficient

$$S^s_{f,f'} = \sum_{b=1}^{B}\psi_b\sqrt{\frac{n_b n'_b}{\left(\sum_b n_b\right)\left(\sum_b n'_b\right)}}, \tag{B4}$$

$$\psi_b = 8\pi|\sigma_b\sigma'_b|^{1/4}N(\mu_b, \mu'_b, 2(\sigma_b + \sigma'_b)), \tag{B5}$$

where $N(a, \mu, \sigma)$ is a two dimensional normal distribution with the expected vector μ and covariance matrix σ, which is evaluated at point a. The correction term ensures that $0 \leq S^s_{f,f'} \leq 1$ and $S^s_{f,f'} = 1$ for any f.[21] Finally, the similarity measure is used to build the RP by Eq. (9) like the mapogram.

APPENDIX C: HIGH DIMENSIONAL RECURRENCE PLOT

In contrast to the spatiogram and the mapogram, here the point wise dissimilarity of two data fields $F(t)$ and $F(t')$ is used to construct an RP.[15] For this purpose, each data field is transformed to a high dimensional vector, $\vec{x}(t) \in \mathbb{R}^{N^2}$. Using this representation, the dissimilarity of two data fields is given by the distance of the corresponding vectors

$$D_{t,t'} = ||\vec{x}(t) - \vec{x}(t')||, \tag{C1}$$

where $||\ldots||$ is a chosen metric. In this work, we use the Euclidean metric, i.e.,

$$D_{t,t'} = \sqrt{\sum_{i=1}^{N_i}\sum_{j=1}^{N_j}(f_{ij}(t) - f_{ij}(t'))^2}. \tag{C2}$$

Finally, the RP is build by

$$R_{t,t'} = \Theta(\epsilon - D_{t,t'}). \tag{C3}$$

[1]P. Eckmann, S. O. Kamphorst, and D. Ruelle, "Recurrence plots of dynamical systems," J. Europhys. Lett. **4**, 973 (1987).
[2]N. Marwan, M. C. Romano, M. Thiel, and J. Kurths, "Recurrence plots for the analysis of complex systems," Phys. Rep. **438**, 237 (2007).
[3]N. Marwan, J. Kurths, and P. Saparin, "Generalised recurrence plot analysis for spatial data," Phys. Lett. A **360**, 545 (2007).
[4]A. Facchini, C. Mocenni, and A. Vicino, "Generalized recurrence plots for the analysis of images from spatially distributed systems," Physica D **238**, 162 (2009).
[5]A. Facchini and C. Mocenni, "Recurrence methods for the identification of morphogenetic patterns," PLoS ONE **8**, e73686 (2013).
[6]C. Mocenni, A. Facchini, and A. Vicino, "Comparison of recurrence quantification methods for the analysis of temporal and spatial chaos," Math. Comput. Modell. **53**, 1535 (2011).
[7]D. B. Vasconcelos, S. R. Lopes, R. L. Viana, and J. Kurths, "Spatial recurrence plots," Phys. Rev. E **73**, 056207 (2006).
[8]T. L. Prado, P. P. Galuzio, S. R. Lopes, and R. L. Viana, "Spatial recurrence analysis: A sensitive and fast detector tool in digital mammography," Chaos **24**, 013106 (2014).

[9]C. Mocenni, A. Facchini, and A. Vicino, "Identifying the dynamics of complex spatio-temporal systems by spatial recurrence properties," Proc. Natl. Acad. Sci. **107**, 8097 (2010).
[10]A. Facchini, F. Rossi, and C. Mocenni, "Spatial recurrence strategies reveal different routes to Turing pattern formation in chemical systems," Phys. Lett. A **373**, 4266 (2009).
[11]R. A. Monserud and R. Leemans, "Comparing global vegetation maps with the kappa statistic," Ecol. Modell. **62**, 275 (1992).
[12]S. T. Birchfield and S. Rangarajan, "Spatiograms versus histograms for region-based tracking," in *Proceedings of the IEEE Computer Society Conference on Computer Vision and Pattern Recognition* (2005), p. 1158.
[13]M. Nilsson, J. S. Bartunek, J. Nordberg, and I. Claesson, "On histograms and spatiograms-introduction of the mapogram," in *Proceedings of the 15th IEEE International Conference on Image Processing, ICIP* (2008), p. 973.
[14]P. Agustí, V. J. Traver, M. J. Marin-Jimenez, and F. Pla, "Exploring alternative spatial and temporal dense representations for action recognition," *Computer Analysis of Images and Patterns*, Lecture Notes in Computer Science Vol. 6855 (Springer, 2011), p. 364.
[15]N. Marwan, J. Kurths, and S. Foerster, "Analysing spatially extended high-dimensional dynamics by recurrence plots," Phys. Lett. A **379**, 894 (2015).
[16]W. Dzwinel, "Spatially extended populations reproducing logistic map," Cent. Eur. J. Phys. **8**, 33 (2010).
[17]B. W. Silverman, *Density Estimation for Statistics and Data Analysis* (CRC press, 1986).
[18]N. Marwan, J. F. Donges, Y. Zou, R. V. Donner, and J. Kurths, "Complex network approach for recurrence analysis of time series," Phys. Lett. A **373**, 4246 (2009).
[19]J. Soto, "Statistical testing of random number generators," in *Proceedings of the 22nd National Information Systems Security Conference* (1999), Vol. 10, p. 12.
[20]L. de Micco, H. A. Larrondo, A. Plastino, and O. A. Rosso, "Quantifiers for randomness of chaotic pseudo-random number generators," Philos. Trans. R. Soc., A **367**, 3281 (2009).
[21]C. O. Conaire, N. E. O'Connor, and A. F. Smeaton, "An improved spatiogram similarity measure for robust object localisation," in *Proceedings of the IEEE International Conference on Acoustics, Speech and Signal Processing, ICASSP* (2007), p. 1.